

The proper motion of stars in dwarf galaxies: distinguishing central density cusps from cores

Ivan de Martino^{1,2*}, Antonaldo Diaferio^{1,3}, Luisa Ostorero^{1,3}

¹ Dipartimento di Fisica, Università di Torino, Via P. Giuria 1, I-10125 Torino, Italy

² Universidad de Salamanca, Facultad de Ciencias., Física Teórica, Salamanca, Plaza de la Merced s/n. 37008, Spain

³ Istituto Nazionale di Fisica Nucleare (INFN), Sezione di Torino, Via P. Giuria 1, I-10125 Torino, Italy

Accepted XXX. Received YYY; in original form ZZZ

ABSTRACT

We show that measuring the proper motion of ~ 2000 stars within a dwarf galaxy, with an uncertainty of 1 km/s at most, can establish whether the Dark Matter (DM) density profile of the dwarf has a central core or cusp. We derive these limits by building mock star catalogues similar to those expected from future astrometric *Theia*-like missions and including celestial coordinates, radial velocity and proper motion of the stars. The density field of the DM halo of the dwarf is sampled from an extended Navarro-Frank-White (eNFW) spherical model, whereas the number density distribution of the stars is a Plummer sphere. The velocity field of the stars is set according to the Jeans equations. A Monte Carlo Markov Chain algorithm applied to a sample of $N \gtrsim 2000$ stars returns unbiased estimates of the eNFW DM parameters within 10% of the true values and with 1σ relative uncertainties $\lesssim 20\%$. The proper motions of the stars lift the degeneracy among the eNFW parameters which appears when the line-of-sight velocities alone are available. Our analysis demonstrates that, by estimating the log-slope of the mass density profile estimated at the half-light radius, a sample of $N = 2000$ stars can distinguish between a core and a cusp at more than 8σ . Proper motions also return unbiased estimates of the dwarf mass profile with 1σ uncertainties that decrease, on average, from 2.65 dex to 0.15 dex when the size of the star sample increases from $N = 100$ to $N = 6000$ stars. The measure of the proper motions can thus strongly constrain the distribution of DM in nearby dwarfs and provides fundamental contribution to understanding the nature and the properties of DM.

Key words: galaxies, dwarf – galaxies, haloes – galaxies, kinematics and dynamics – galaxies, proper motions – Astrometry and celestial mechanics, statistical – methods

1 INTRODUCTION

Indirect observational pieces of evidence suggesting the existence of dark matter (DM) have been accumulating over the last decades (see, e.g., Salucci 2018, and references therein). DM is suggested to be made of particles emerging from the supersymmetric extensions of the standard model (Ellis et al. 1984); these hypothetical particles are weakly interacting with standard matter, they are non-relativistic and basically collisionless (for comprehensive reviews see, e.g., Bertone et al. 2005; Feng 2010; Frenk & White 2012; Primack 2012; Freese 2017; Bertone & Hooper 2018). This Cold Dark Matter (CDM) paradigm successfully explains the evolution and formation of the large-scale structure (e.g., Planck Collaboration et al. 2020). However, a direct detection of dark matter particles is still missing (Akerib et al. 2017; Aprile et al. 2018; Tanabashi et al. 2018). In addition, the CDM model shows some tensions with observations both at cosmological scales (Planck Collaboration et al. 2016; Riess

et al. 2016; Schwarz et al. 2016; Riess et al. 2019; Di Valentino et al. 2020; Mathews et al. 2020; Handley 2021; Luongo et al. 2021) and at galactic scales (Weinberg et al. 2015; Del Popolo & Le Delliou 2017; Bullock & Boylan-Kolchin 2017; De Martino et al. 2020a).

Among the latter tensions, the core-cusp problem (CCP) is the discrepancy between the inner slope of the DM density profile of galaxies, inferred from observations, and the profile that is predicted by DM-only N-body simulations (e.g., Navarro et al. 1997): large cores appear to be commonly present in real dwarf galaxies (Carignan & Freeman 1988; Carignan & Beaulieu 1989; De Blok & McGaugh 1997; Mateo 1998; De Blok & McGaugh 1997; Gentile et al. 2007; Oh et al. 2015; Torrealba et al. 2016; Caldwell et al. 2017; Torrealba et al. 2019), whereas N-body simulations predict that DM haloes should have a central density cusp. Although hydrodynamical simulations, that include dissipative processes, suggest that energy feedback from stars, supernovae explosions, and high-energy phenomena may turn the cusp of the DM profile into a core (Mashchenko et al. 2008; Pontzen & Governato 2012; Governato et al. 2012; Oñorbe et al. 2015; Read et al. 2016), more

* E-mail: ivan.demartino@usal.es

recent hydrodynamical simulations seem to disfavour this and related mechanisms (Benítez-Llambay et al. 2019; Bose et al. 2019).

A more drastic solution might require a change in the CDM paradigm. This change may involve either the nature of the dark matter particles, for example the replacement of the CDM particles with self-interacting dark matter (Rocha et al. 2013) or ultra-light axions (Chen et al. 2017; Broadhurst et al. 2020; Pozo et al. 2021), or a modification of the theory of gravity (e.g., Famaey & McGaugh 2012; De Martino 2016; De Martino & De Laurentis 2017; Del Popolo & Le Delliou 2017; De Martino 2020).

Self-interacting DM, rather than CDM, can provide a solution to the CCP by generating a central core without resorting to baryonic feedback (e.g. Spergel & Steinhardt 2000; Rocha et al. 2013). A similar solution can be provided by fuzzy DM, where the DM particles are very light bosons with mass $\sim 10^{-22}$ eV (Hu et al. 2000; Chen et al. 2017; Broadhurst et al. 2020; De Martino et al. 2020b; Pozo et al. 2021). Berezhiani & Houry (2015) proposed that DM made of axion-like particles can actually be a superfluid on galactic scales and keep the collisionless behaviour of standard CDM on larger scales. The additional force induced by this superfluid DM on galactic scales appears to be consistent with the observed phenomenology of galaxies, some of which appears problematic for the standard CDM model but was largely predicted by Modified Newtonian Dynamics (MOND) (Milgrom 1983; Bekenstein & Milgrom 1984; Famaey & McGaugh 2012; McGaugh 2020).

On the observational side, the presence of cores rather than cusps is still disputed (Van den Bosch & Swaters 2001; Spekkens et al. 2005; Walker et al. 2009; Di Cintio et al. 2014; Marsh & Pop 2015). Indeed, current data appear unable to unambiguously distinguish between a central cusp and a core in dark matter density profiles (e.g., Walker et al. 2009). Although the recent discoveries of ultra-faint galaxies seem to suggest the existence of a large core in their innermost region on the basis of their velocity dispersion profile (see for instance Torrealba et al. 2019), the constraining power of these observations is weak and the debate on whether dwarf galaxies do or do not exhibit a large dark matter core is still open.

The method to map the distribution of DM depends on the type of system under investigation: for a rotationally-supported galaxy, the DM distribution is generally inferred from the fit to the rotation curve, whereas, for a pressure-supported dwarf spheroidal galaxy, we rely on the profile of the line-of-sight velocity dispersion, if no other data set, like multiple stellar populations (e.g., Walker et al. 2009; Walker & Peñarrubia 2011), proper motions (e.g., Strigari et al. 2007; Evslin 2015), or three dimensional positions (e.g., Richardson et al. 2014) is available.

The standard approach is to assume a functional form for the DM halo density profile and determine its parameters from a fit to the data. Unfortunately, this approach generally suffers from degeneracies among the parameters of the DM density profile and even among them and other unknown parameters (Lokas 2002; De Lorenzi et al. 2009; Walker et al. 2009; Napolitano et al. 2014; Read & Steger 2017). A well-known case is the degeneracy between the velocity anisotropy parameter β and the total halo mass in the Jeans equations (e.g., Lokas 2002; Binney & Tremaine 2008; Campbell et al. 2017). This drawback may inhibit the distinction between models with a cusp and with a core, as it happens when fitting the line-of-sight velocity dispersion profiles of the Milky Way satellites (Walker et al. 2009; Breddels & Helmi 2013; Richardson & Fairbairn 2013). This degeneracy can be lifted by adding information from multiple stellar populations (e.g., Walker & Peñarrubia 2011; Zhu et al. 2016a,b) or higher velocity moments (e.g., Lokas

& Mamon 2003). However, N-body simulations show that multiple stellar populations only partially lift the degeneracy, whereas higher velocity moments combined with proper motions appear to be more effective (Read & Steger 2017; Webb & Vesperini 2018). Massari et al. (2018, 2020) use the proper motions of only a few hundred stars to estimate the velocity anisotropy parameter $\beta = 0.86^{+0.12}_{-0.83}$ and $\beta = 0.25^{+0.47}_{-1.38}$ in the Sculptor and Draco dwarf galaxies, respectively.

Here, we quantify how proper motions can indeed lift the mass-anisotropy degeneracy and shed light on the CCP in dwarf galaxies. The proper motions of the stars of the dwarf combined with their line-of-sight velocities from their spectra provide the three-dimensional velocity field within the dwarf. Strigari et al. (2007) pointed out that adding the proper motion of 200 stars to their line-of-sight velocity would make it possible to constrain the log-slope of the DM density profile at twice the King radius with 20% statistical uncertainty, whereas using only the line-of-sight velocities leaves the log-slope parameter unconstrained.

More recently, Watkins et al. (2013) (hereafter W13) suggested a procedure to model proper motion data sets in axisymmetric systems, and applied their approach to the star cluster ω -Centauri.¹ By assuming that the velocity distribution of the stars in the system is described by a trivariate Gaussian, W13 constructed a probability distribution function of the 3-dimensional velocity field based on the solution of the Jeans equations that can be applied to discrete velocity data. In this technique, Zhu et al. (2016a) included a chemo-dynamical model with multiple stellar populations. Zhu et al. (2016b) (hereafter Z16) applied this combined technique to a star catalogue of the Sculptor dwarf spheroidal; they use mock data to estimate that a dataset of approximately 6000 stars with line-of-sight velocities and metallicity information but no proper motions is required to solve the CCP.

Here, we assume a single population of stars with no metallicity information and perfectly known celestial coordinates and adopt the approach of W13 to estimate the parameters of the DM density profile based on kinematical information alone. We create mock data sets mirroring the generic expected observational limitations of future space-borne astrometric missions to determine the minimum number of stars and the maximum uncertainty on the proper motions that are required to effectively solve the CCP. As a benchmark, we adopt a future *Theia*-like mission (Malbet et al. 2016; The *Theia* Collaboration et al. 2017; Malbet et al. 2019; Malbet et al. 2021) designed to achieve an end-of-mission uncertainty on proper motions of a few $\mu\text{s yr}^{-1}$, namely ~ 100 times smaller than the uncertainty of *Gaia* (Gaia Collaboration 2016; Gaia Collaboration et al. 2016a,b, 2018b,a, 2021). A *Theia*-like mission is thus expected to be able to measure the proper motions of stars in nearby dwarf galaxies, and thus solve the CCP through an accurate determination of the DM density profile. A solution to the CCP based on proper motions may also be provided by future 30 meter class telescopes as, e.g., the Thirty Meter Telescope (TMT)² (Schoeck et al. 2013; Skidmore et al. 2015), or by a combination of measures from these telescopes and space-based facilities (Evslin 2015).

¹ By adopting the approach of Watkins et al. (2013), Evans et al. (2022) use the most recent kinematic data of ω -Centauri to constrain both the distribution of the non-luminous mass component of this globular cluster and, if this dark component is made of elementary particles, the J-factor associated with the observable flux of γ -rays coming from dark matter particle annihilations.

² <http://www.tmt.org>

Section §2 describes the mock catalogues and Section §3 our methodology for the data processing. Section §4 shows how our procedure is effective in constraining the model parameters and solving the CCP. Section §5 explores the dependence of the accuracy of the estimated cumulative mass profile of the dwarf on the size of the star sample and on the knowledge of proper motions. We summarize our results and conclude in Section §6.

2 METHOD

The creation of an astrometric mock catalogue of the stars in a dwarf galaxy requires the assumption of the phase-space distributions of both the stellar and the DM components, and the sampling of the stellar distribution. We adopt two assumptions: (1) both the DM and the star distributions are spherically symmetric; (2) the anisotropy velocity parameter β is independent of radius.

2.1 Stellar Distribution

Following Walker et al. (2009), for the stellar number density distribution we adopt the Plummer (1911) model

$$\nu(r) \propto \left(1 + \frac{r^2}{a^2}\right)^{-5/2}, \quad (1)$$

where a is a scale length. The stellar mass density is proportional to $\nu(r)$. In dwarf spheroidal galaxies, DM dynamically dominates over the stellar mass density component at any radius, including the central regions (e.g., De Martino et al. 2020a, and references therein); therefore, the stellar contribution to the total gravitational dynamics is negligible. Hereafter, we thus ignore the contribution of the stars to the dynamics of the dwarf.

2.2 Dark matter distribution

We model the DM mass density distribution with the profile (Hernquist 1990; Zhao 1996)

$$\rho(r) = \rho_0 \left(\frac{r}{r_s}\right)^{-\gamma} \left[1 + \left(\frac{r}{r_s}\right)^\alpha\right]^{\frac{\gamma-\delta}{\alpha}}. \quad (2)$$

The free parameters are the central density ρ_0 , the scale radius r_s , and the three slope parameters α , δ , and γ .³ The value $\gamma = 0$ corresponds to a density profile with a central core, whereas $\gamma > 0$ indicates a profile with a cusp. Equation (2) defines an extended Navarro-Frenk-White (eNFW) profile and reduces to the standard Navarro-Frenk-White profile (Navarro et al. 1997) when $(\alpha, \delta, \gamma) = (1, 3, 1)$. In our models, we always set $\alpha = 1$ and $\delta = 3$. We explore the profiles with a core and with a cusp by setting $\gamma = 0$ and $\gamma = 1$, respectively, similarly to Walker et al. (2009).

With the density profile of Eq. (2), the cumulative mass within radius r is

$$M(< r) = \frac{4\pi\rho_0 r_s^3}{3-\gamma} \left(\frac{r}{r_s}\right)^{3-\gamma} {}_2F_1\left(3-\gamma, 3-\gamma; 3-\gamma+1; -\frac{r}{r_s}\right), \quad (3)$$

where ${}_2F_1$ is the hypergeometric function.

³ The parameter δ is usually called β . Here, we adopt a different notation to avoid confusion with the velocity anisotropy parameter β appearing in the Jeans equations.

2.3 Sampling the phase-space distributions

We consider a sample of N stars with spherical coordinates (r, θ, ϕ) in the reference frame centered on the centre of mass of the dwarf: the radius r derives from sampling the Plummer density profile of Eq. (1), whereas the angular coordinates are sampled from uniform distributions in the ranges $\cos \theta = (-1, 1)$ and $\phi = (0, 2\pi)$.

We sample the three velocity components of each star from the velocity distribution function, assumed to be a multivariate Gaussian distribution. The probability of finding a velocity v at position r is thus

$$p(v|r) = \frac{\exp\left\{-\frac{1}{2} [v - \mu(r)]^T C^{-1}(r) [v - \mu(r)]\right\}}{\sqrt{(2\pi)^3 |C(r)|}}, \quad (4)$$

where

$$\mu(r) = \begin{pmatrix} \overline{v_x} \\ \overline{v_y} \\ \overline{v_z} \end{pmatrix} \quad (5)$$

is the mean velocity at position r , and

$$C(r) = \begin{pmatrix} \overline{v_x^2} - \overline{v_x}^2 & \overline{v_{xy}^2} - \overline{v_x} \overline{v_y} & \overline{v_{xz}^2} - \overline{v_x} \overline{v_z} \\ \overline{v_{xy}^2} - \overline{v_x} \overline{v_y} & \overline{v_y^2} - \overline{v_y}^2 & \overline{v_{yz}^2} - \overline{v_y} \overline{v_z} \\ \overline{v_{xz}^2} - \overline{v_x} \overline{v_z} & \overline{v_{yz}^2} - \overline{v_y} \overline{v_z} & \overline{v_z^2} - \overline{v_z}^2 \end{pmatrix} \quad (6)$$

is the covariance matrix at the same position r . In the above equations, the x , y , and z subscripts denote the Cartesian coordinates in the reference frame of the dwarf. The x and y axes lie on the plane of the sky, while the z axis is set along the line of sight. The quantities $\overline{v_x}$ and $\overline{v_x^2}$ are the first and second moments of the velocity distribution in the direction of the x axis, and a similar convention is adopted for the other moments and directions. The equations of transformation of the star velocity from the Cartesian coordinate system, as shown in Eqns. (4)-(6), to the spherical coordinate system are provided in Appendix A.

In spherical symmetry, we have $\overline{v_r} = \overline{v_\theta} = \overline{v_\phi} = 0$ and $\overline{v_r v_\theta} = \overline{v_r v_\phi} = \overline{v_\theta v_\phi} = 0$, and the radial component of the Jeans equation reads

$$\frac{1}{v(r)} \frac{d[v(r)\overline{v_r^2}(r)]}{dr} + 2\beta(r) \frac{\overline{v_r^2}(r)}{r} = -\frac{d\Phi(r)}{dr}, \quad (7)$$

with $\Phi(r)$ the gravitational potential. We further simplify our model by assuming that the velocity anisotropy parameter

$$\beta(r) = 1 - \frac{\overline{v_\theta^2}(r) + \overline{v_\phi^2}(r)}{2\overline{v_r^2}(r)} = 1 - \frac{\overline{v_t^2}(r)}{\overline{v_r^2}(r)} \quad (8)$$

is independent of r . In the equation above, $\overline{v_\theta^2}(r) = \overline{v_\phi^2}(r)$ and $\overline{v_t^2}(r) \equiv [\overline{v_\theta^2}(r) + \overline{v_\phi^2}(r)]/2$. The general solution of the Jeans equation is thus

$$\overline{v_r^2}(r) = \frac{1}{v(r)r^{2\beta}} \int_r^\infty dr' r'^{2\beta} v(r') \frac{d\Phi}{dr'}. \quad (9)$$

Given $v(r)$ and $\rho(r)$ from Eqns. (1) and (2) and for a chosen value of β , Eq. (9) returns the covariance matrix $C(r)$ in Eq. (6) once converting from spherical to Cartesian coordinates. We can now sample the three velocity components from the velocity distribution function in Eq. (4).

Table 1. Parameters of the mock stellar catalogues. The three listed values of β and σ_v are adopted for both the core and cusp models.

Parameters		Values		Unit
Name	Description	Core	Cusp	
ρ_0	DM central density	192.42	5.38	$10^7 M_\odot \text{kpc}^{-3}$
r_s	DM scale radius	150	795	pc
α	DM slope	1	1	
δ	DM slope	3	3	
γ	DM slope	0	1	
a	stellar scale radius	196	196	pc
β	velocity anisotropy	{-0.25, 0, 0.25}		
σ_v	velocity uncertainty	{0.0, 1.0, 5.0}		km s^{-1}

2.4 Test of the sampling

To test our procedure to create the simulated dwarf, we compare the cumulative number of stars of our sample with the cumulative number expected from a Plummer sphere

$$N_{\text{th}}(<r) = \frac{Nr^3}{(r^2 + a^2)^{3/2}}, \quad (10)$$

where N is the total number of stars in the sample. The upper panel of Fig. 1 shows the comparison for a sample of $N = 6000$ stars in a DM density profile with a core, $\gamma = 0$, and isotropic velocity field, $\beta = 0$. We adopt equally-spaced radial bins, each containing $N_{b,k}$ stars. The statistical fluctuation on the observed number of stars in the k -th bin is

$$\sigma_{N_{b,k}} = N_{b,k}^{1/2}. \quad (11)$$

The corresponding error bars are not visible in the figure because they are smaller than the symbol size. The agreement between our sampling and the expected profile is within the fluctuations due to shot noise. Samples with smaller N show similar results.

The lower panel of Fig. 1 compares the expected radial velocity dispersion profile [see Eq. (9)] with the velocity dispersion of the same sample of $N = 6000$ stars. By associating each star with radial velocity $(v_r)_i$ to the proper k -th radial bin, the radial velocity dispersion profile is

$$\overline{v_{r,k}^2}^{1/2}(r) = \left[\sum_i^{N_{b,k}} (v_r)_i^2 / N_{b,k} \right]^{1/2}. \quad (12)$$

The statistical fluctuation on the velocity dispersion profile in each bin is

$$\sigma_{\overline{v_{r,k}^2}^{1/2}} = \left[\frac{\overline{v_{r,k}^2}}{2(N_{b,k} - 1)} \right]^{1/2}. \quad (13)$$

Similarly to the density profile, the agreement between our sampling and the expected profile is within the fluctuations due to shot noise and supports the validity of our sampling procedure.

2.5 Astrometric mock catalogues

We assume that, for each star in the dwarf, the astrometric catalogue lists the two celestial coordinates, the velocity component along the line of sight, and the two components of the proper motion. With the known distance between the observer and the dwarf, the two celestial coordinates return the projected radial distance R of the star from the centre of the dwarf. Similarly, by assuming that all the stars are at the same distance from the observer, namely by neglecting the size of the dwarf along the line of sight, we can derive the three

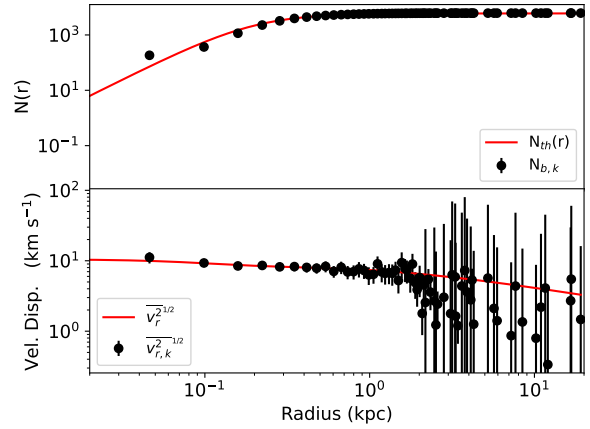


Figure 1. Example of the sampling of a dwarf with a core and isotropic velocity field $\beta = 0$ with a mock catalogue with 6000 stars. *Upper panel:* The cumulative number of stars in the sample (black points) and the number expected from a Plummer sphere according to Eq. (10) (red solid line). *Lower panel:* The radial velocity dispersion profile according to Eq. (9) (red solid line) and Eq. (12) (black points).

velocity components in the reference frame of the dwarf from the components of the proper motion and from the line-of-sight velocity component.

In our mock catalogues, for each star, we list the projected radial distance R and the three velocity components v_x , v_y , and v_z in the reference frame of the dwarf. We thus assume that the distance to the dwarf is known without uncertainty and that we have already transformed the observable quantities into the phase-space coordinates in the dwarf reference frame.

Table 1 lists the parameters we adopt to build our galaxy models. The DM parameters and the Plummer scale length are from Table 3 and Table 1, respectively, of Walker et al. (2009). These parameters correspond to Draco galaxy. We adopt this dwarf as a working example of the possible targets of future *Theia*-like astrometric missions (Malbet et al. 2016; The Theia Collaboration et al. 2017; Malbet et al. 2019; Malbet et al. 2021).

We create the mock catalogues of a dwarf whose DM density profile has either a core ($\gamma = 0$) or a cusp ($\gamma = 1$). We consider three different values of the velocity anisotropy parameter β ; these values are consistent with $\beta = 0.25^{+0.47}_{-1.38}$ as measured by Massari et al. (2020) for Draco.

Figure 2 shows the density and velocity dispersion profiles of our models. The density profile in the left panel shows that the two density profiles differ by 10% at the half-light radius $r_{1/2} = a$. The profiles of the velocity dispersion projected along the line of sight differ, in the two models, by $\sim 2\%$, $\sim 2.6\%$ and $\sim 3\%$ within $r_{1/2}$ when $\beta = 0.25, 0.0$ and -0.25 respectively; the difference substantially increases at larger radii. We do not show the profiles of the velocity dispersion of the proper motions which are qualitatively similar to the profiles of the velocity dispersion along the line of sight. The difference in the velocity dispersion profiles at large radii shows the relevance of the measure of the velocity field to distinguish between core and cusp models.

We consider five different sizes of the star samples: $N = 100, 1000, 2000, 4000,$ and 6000 . The largest sample size, $N = 6000$, is set according to Z16, who found that this minimum number of stars is required to distinguish between a core and a cusp if the line-of-

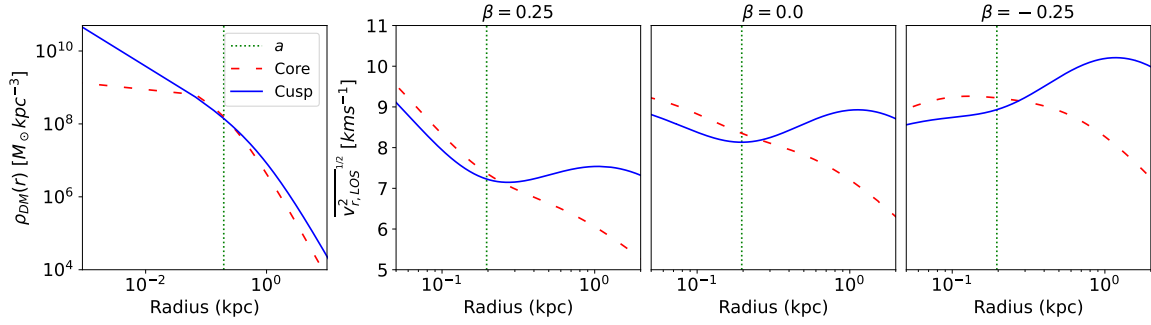


Figure 2. Density profile (left panel) and velocity dispersion profiles projected along the line of sight (the three right panels) of our fiducial models. The solid blue and dashed red lines refer to the model with the central cusp and the central core respectively. The vertical green dotted lines show the location of the half-light radius $r_{1/2} = a$, where a is the scale radius of the Plummer model of Eq. (1). The value of the velocity anisotropy parameter β is indicated on top of each of the three right panels.

Table 2. Priors of our Bayesian procedure adopted to recover the parameters of our dwarf model. U indicates a uniform distribution in the range indicated in brackets.

Parameter		Prior
$\log_{10}\left(\frac{\rho_0}{10^7 M_\odot/\text{kpc}^3}\right)$	DM central density	$U(-3, 5)$
$\log_{10}\left(\frac{r_s}{\text{kpc}}\right)$	DM scale radius	$U(-2, 3)$
γ	central DM slope	$fU(-3, 3)$
β	velocity anisotropy	$U(-10, 1)$

sight velocities alone are available and the sample can be separated into two stellar populations according to the metallicity of the stars.

Finally, we consider three different observational uncertainties σ_v on the velocity measures, namely 0.0, 1.0, and 5.0 km s⁻¹. For any star in our sample, these uncertainties are associated to every Cartesian velocity component. This assumption is clearly unrealistic, and is made for the sake of simplicity. Indeed, (i) the uncertainties on the velocity components of a star depend on the star brightness, and (ii) different velocity components are measured with different techniques, either astrometric or spectroscopic, and thus suffer from different uncertainties.

At the distance of Draco, ~ 76 kpc (e.g., [McConnachie 2012](#)), the uncertainty $\sigma_v = 1.0$ km s⁻¹ implies an uncertainty $\sim 4 \mu\text{as yr}^{-1}$ on the proper motion of a star. This uncertainty is comparable to the precision of a few $\mu\text{as yr}^{-1}$ expected for *Theia*-like astrometric missions ([Malbet et al. 2019](#); [Malbet et al. 2021](#)).

3 DATA PROCESSING

The goal of our analysis is to determine the minimum size of the sample of stars and the minimum uncertainty on the proper motions that are required to properly recover the parameters of the DM distribution. We adopt a Bayesian approach.

We use the Monte-Carlo-Markov-Chain (MCMC) software emcee ([Foreman-Mackey et al. 2013](#)). The four parameters that completely describe our models are the DM central density, ρ_0 , the DM scale length, r_s , the slope of the inner DM density profile, γ , and the velocity anisotropy, β . They define the four-dimensional vector $\mathbf{f} = (\rho_0, r_s, \gamma, \beta)$. Note that, with our simplified approach, we do not explore the determination of the slope parameters α and δ [Eq. (2)] that we unrealistically assume to be known.

To speed up the chain convergence and reduce the burn-in

phase, we first run 100 chains with randomly chosen starting points in the parameter space. For each component of \mathbf{f} , we adopt a flat prior distribution within the ranges listed in Table 2. We run all the chains for 500 steps; we then identify the point in the four-dimensional parameter space that, over all the 100 chains, has the largest probability. We consider a four-dimensional cubic volume centered on this point. In each dimension, the cube has a side 0.2 times the value of the coordinate of the point in that dimension. Finally, we randomly choose $N_c = 32$ points within this volume. We adopt these points as the starting points of the 32 new chains of our final analysis. We verify that this initial procedure speeds up the convergence of the 32 chains without affecting the estimation of the posterior distributions of the model parameters.

We guarantee the convergence of all the 32 chains at the same time as follows. For each j -th chain, at each step N , we consider the average value $\mu_{\mathbf{f}}^j$ of the values \mathbf{f}_i^j estimated in all the previous steps,

$$\mu_{\mathbf{f}}^j = \frac{1}{N} \sum_{i=1}^N \mathbf{f}_i^j. \quad (14)$$

We then estimate the autocorrelation function as a function of the lag τ ,

$$\hat{C}_{\mathbf{f}}^j(\tau) = \frac{1}{N - \tau} \sum_{i=1}^{N-\tau} (\mathbf{f}_i^j - \mu_{\mathbf{f}}^j) (\mathbf{f}_{i+\tau}^j - \mu_{\mathbf{f}}^j), \quad (15)$$

that, in turn, provides the normalized autocorrelation function averaged over the number of chains N_c ,

$$\hat{\rho}_{\mathbf{f}}(\tau) = \frac{1}{N_c} \sum_{j=1}^{N_c} \frac{\hat{C}_{\mathbf{f}}^j(\tau)}{\hat{C}_{\mathbf{f}}^j(0)}. \quad (16)$$

We can now estimate the autocorrelation time for the vector \mathbf{f} ,

$$\hat{\tau}_{\mathbf{f}}(M) = 1 + 2 \sum_{\tau=1}^M \hat{\rho}_{\mathbf{f}}(\tau), \quad (17)$$

where $M < N$.

We check $\hat{\tau}_{\mathbf{f}}$ every 100 steps. The chains converge when two conditions are satisfied at the same time and for all the components of \mathbf{f} : (1) all the chains are longer than 100 times the autocorrelation time, and (2) the autocorrelation time has changed by less than 1%.

The likelihood function is

$$\mathcal{L} = \prod_{i=1}^n p(\mathbf{v}_i | \mathbf{r}_i), \quad (18)$$

where i denotes the i -th star in the data set, and

$$p(v|\mathbf{r}) = \frac{\exp\left\{-\frac{1}{2} [v - \boldsymbol{\mu}(\mathbf{r})]^T [C(\mathbf{r}) + S(\mathbf{r})]^{-1} [v - \boldsymbol{\mu}(\mathbf{r})]\right\}}{\sqrt{(2\pi)^n |C(\mathbf{r}) + S(\mathbf{r})|}} \quad (19)$$

is the convolution between the Gaussian distribution with covariance matrix $\mathbf{S}(\mathbf{r})$, representing the instrumental errors, and the Gaussian distribution with covariance matrix $\mathbf{C}(\mathbf{r})$ representing the probability distribution of the velocity components given in Eq. (4).

If the measurements are uncorrelated, the off-diagonal elements of $\mathbf{S}(\mathbf{r})$ are equal to zero and the diagonal components of $\mathbf{S}(\mathbf{r})$ are the squared errors of the error measurements: $\{\sigma_{v_x}^2, \sigma_{v_y}^2, \sigma_{v_z}^2\}$. We assume no error on the positions.

As anticipated in Sect. 2.5, we consider mock catalogues with velocity uncertainty $\sigma_v = 0.0, 1.0, \text{ or } 5.0 \text{ km s}^{-1}$ on each of the three Cartesian velocity components: $\sigma_{v_x} = \sigma_{v_y} = \sigma_{v_z} \equiv \sigma_v$. We do not model any dependence of the velocity uncertainty on the star magnitude. For reference, Z16 perturbed the stars in their sample with an error of 3 km s^{-1} .

4 RESULTS

Here, we show the results of the MCMC analysis of our mock catalogues. As a test case, in Sect. 4.1 we show the results of a dwarf galaxy with a core, $\gamma = 0$, and isotropic velocity field, $\beta = 0$: this analysis assesses the constraining power of the proper motions of the stars. We then explore how well our MCMC approach can estimate the model parameters for galaxies with either a cusp or a core and with three different values of the velocity anisotropy parameter β . In Sect. 4.2, we explore how the measurement of the proper motion is relevant to solve the CCP.

4.1 Estimation of the parameters of the DM distribution and of the velocity field

In our MCMC analysis, we run 32 chains with random starting points in the parameter space as illustrated in the previous section. Examples of the post burn-in posterior density distributions of the parameters are shown in Fig. 3. This figure shows the case of a mock catalogue with 2000 stars and no errors on the velocity measures. Table 3 lists the results of the MCMC analyses of our full set of mock catalogues for a dwarf with a core, $\gamma = 0$, and an isotropic velocity field, $\beta = 0$. We adopt the medians of the posterior distributions as the best estimates of the parameters; the 15.9 and 84.1 percentiles of the posterior distributions yield the 1σ uncertainties of these estimates.

Figure 3 shows that the posterior distributions of the individual parameters are approximately Gaussian, although some of the distributions show substantial skewness and extended tails; the parameters of the density profile, ρ_0 , r_s , and γ , are degenerate. The degeneracy between ρ_0 and r_s is in agreement with the results of Z16. Nevertheless, for $N \geq 2000$ stars, the MCMC analysis returns the estimates of these parameters within 1σ of the input value (Table 3).

Figure 4 shows how the 1σ confidence interval of the parameter estimates depends on the size N of the star catalogue and on the uncertainty σ_v of the velocity measures. Clearly, when $N \leq 1000$, the MCMC analysis is unable to recover the input parameters. On the contrary, the estimated parameters converge to the input values

when $N \geq 2000$. The convergence is more evident for the velocity anisotropy parameter β .

By measuring the proper motions of 45 stars in Draco, with the combination of *Hubble Space Telescope* observations and the second *Gaia* Data Release, Massari et al. (2020) estimate the velocity anisotropy parameter $\beta = 0.25^{+0.47}_{-1.38}$. These uncertainties agree with the expected errors on β for our mock catalogue with $N = 100$ stars. Our analysis shows that reducing the uncertainty by a factor of ten requires a number of stars at least 20 times larger.

Table 3 shows that, when $N \geq 2000$, the velocity uncertainty σ_v within the range we explore has a moderate impact on the uncertainty of the parameter estimates. For these large sample sizes, the estimated values are unbiased and within $\sim 10\%$ of the input values; in addition, the 1σ uncertainties are generally smaller than $\sim 20\%$.

Figures 5 and 6 show the results obtained when we apply our methodology to our mock catalogues of a dwarf model with three different values of β and with either a cusp or a core in the density profile. In addition, the results shown in these figures assume $\sigma_v = 0 \text{ km s}^{-1}$. According to Table 3, larger uncertainties on the velocities decrease the precision of the estimated parameters but leave the estimates unbiased. The size of the star catalogues appears more relevant than the velocity uncertainty σ_v .

Figures 5 and 6 show that, when the catalogue contains at least $N = 2000$ stars, the input parameters are satisfactorily recovered for any model. Table 4 lists the estimates of the parameters for the catalogues with $N = 2000$ stars.

Table 4 shows that samples of 2000 stars can return the estimate of the central density ρ_0 with a relative error $\sim 15\%$ if the density profile has a core, and a relative error $\sim 30 - 60\%$ if the density profile has a cusp. These uncertainties are consistent with those estimated by Read et al. (2018), who combined ~ 2500 stars with photometric information and ~ 500 stars with measured line-of-sight velocity components to measure the DM density within 150 pc of the centre of Draco. Our analysis suggests that these uncertainties can be reduced by a factor $\sim 1.5 - 2$, with a sample of 6000 stars.

4.2 Distinguishing between a cusp and a core

We now show how the measures of the proper motions of the stars can in principle distinguish between a cusp and a core independently of the specific value of the velocity anisotropy parameter. We consider two identical models except for the value of γ . We set the velocity anisotropy parameter $\beta = 0$, and the velocity uncertainties $\sigma_v = 0 \text{ km s}^{-1}$. The green shaded areas in the left panels of Fig. 7 show the posterior distributions of the recovered parameters of the DM density profile with a core, $\gamma = 0$, derived with our MCMC analyses of a mock catalogue with $N = 6000$ stars. The blue shaded areas show the results for the same case but with a cusp, $\gamma = 1$.

For catalogues of this size, our MCMC analysis returns the estimates $\gamma = 0.20^{+0.26}_{-0.28}$ and $\gamma = 0.90 \pm 0.08$ for the model with a core and with a cusp, respectively. In other words, this result indicates that our MCMC analysis would distinguish between a cusp and a core: if the dwarf has a cusp, a core can be ruled out at largely more than 3σ . We can actually do better: according to the suggestion of Strigari et al. (2007) (see also Guerra et al. 2021), the log-slope $\lambda(r) = -d \ln \rho / d \ln r$, estimated at the half-light radius $r_{1/2}$, can distinguish the two density profiles more efficiently than the measure of γ alone. For our density profile in Eq. (2), $\lambda(r) = \gamma - (\gamma - \delta)(r/r_s)^\alpha / [1 + (r/r_s)^\alpha]$, and for the Plummer stellar density distribution of Eq. (1), $r_{1/2} = a$. In our fiducial models, we thus find $\lambda(a) = 1.70$ and 1.40 for the profiles with a

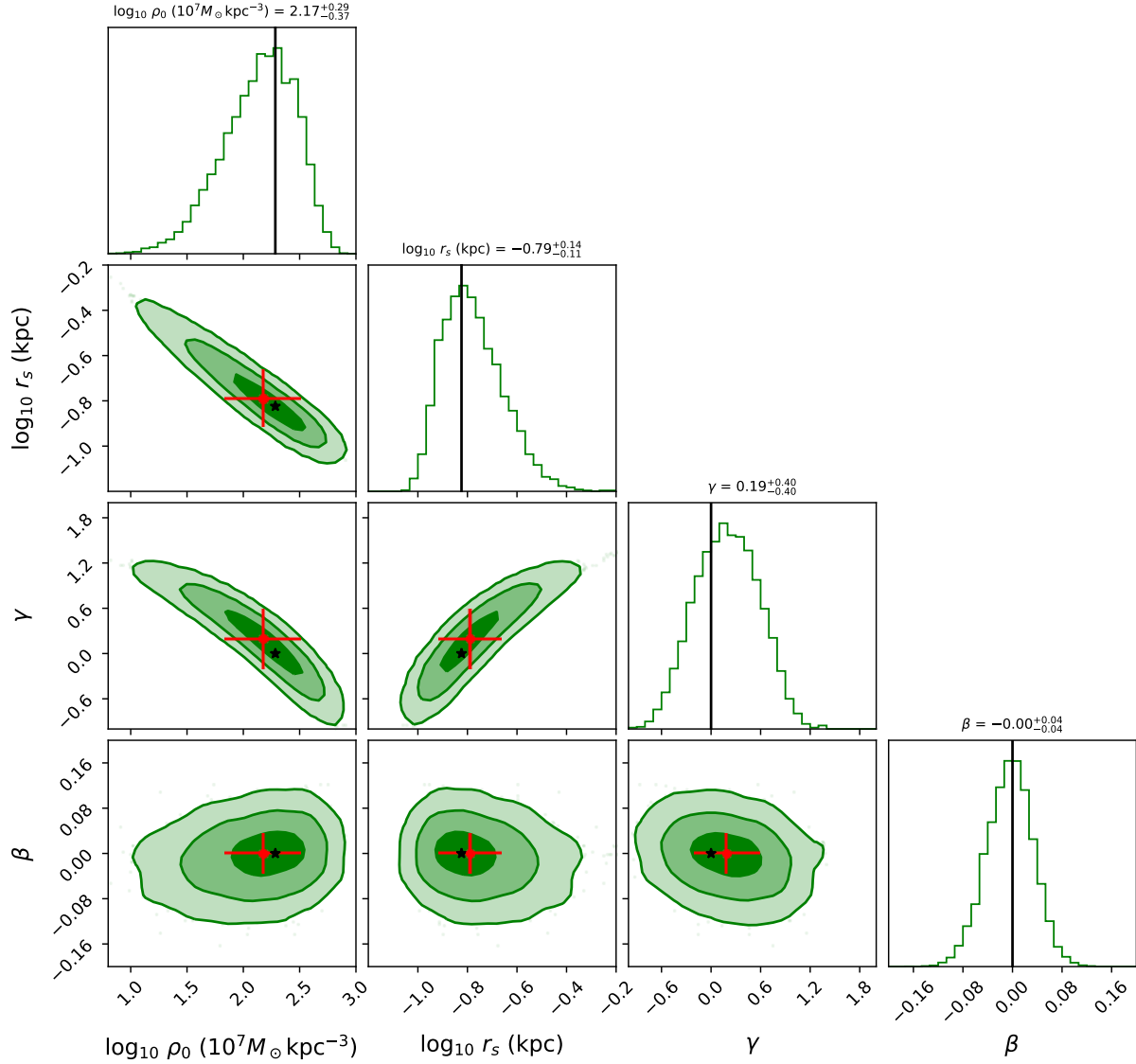


Figure 3. MCMC posterior distributions of the parameters of the model with a core, $\gamma = 0$, and an isotropic velocity field, $\beta = 0$, estimated from a mock sample with $N = 2000$ stars and uncertainty on each velocity component of the stars $\sigma_v = 0 \text{ km s}^{-1}$. The shaded areas with increasing darkness show the 99%, 95%, and 68% confidence regions of the posterior distributions, respectively. The black solid stars show the position of the input parameters used to create the mock catalogue. The input parameters are also indicated by the vertical lines in the top panel of each column. The red solid circles with the error bars are the medians of the posterior distributions with their 68% confidence intervals; they are adopted as the estimated values of the parameters and their uncertainty. These values are reported at the top of each column.

core and a cusp, respectively. The last row of the panels of Fig. 7 shows the posterior distributions of λ . With a sample of 6000 stars, the two models can now be unambiguously distinguished at 16σ .

An anisotropic velocity field increases the separation between the two density models. With a mock catalogue of 6000 stars with $\beta = -0.25$, we find $\gamma = -0.44^{+0.25}_{-0.23}$ and $\gamma = 0.90 \pm 0.07$ for the model with a core and with a cusp, respectively. With $\beta = 0.25$, we get $\gamma = -0.08^{+0.30}_{-0.31}$ and $\gamma = 1.10 \pm 0.08$, respectively. For both values of β , we would thus distinguish the two models at more than 3σ . As for λ , with $\beta = -0.25$, we find $\lambda = 1.69^{+0.02}_{-0.03}$ and $\lambda = 1.34 \pm 0.02$ for the model with a core and with a cusp, respectively. With $\beta = 0.25$, we get $\lambda = 1.73^{+0.02}_{-0.03}$ and $\lambda = 1.42^{+0.02}_{-0.03}$, respectively. For

both values of β , we can now distinguish the two models at more than 10σ .

The right panels of Fig. 7 show the MCMC analysis of the same two models but with fewer stars, $N = 2000$. The estimates of the central slope of the density profiles are now $\gamma = 0.19 \pm 0.40$ and $\gamma = 0.97 \pm 0.11$ for the model with a core and with a cusp, respectively. With this smaller sample of stars, limiting the analysis to the values of γ might thus distinguish the two models at $\sim 2\sigma$. On the contrary, the measure of the log-slope, $\lambda = 1.73 \pm 0.04$ and 1.38 ± 0.04 for the model with a core and a cusp respectively, distinguishes the two models at more than 8σ . The separation between the posterior distributions of λ shown in the right panel of Fig. 7 might suggest that a sample size even smaller than $N = 2000$ would distinguish a

Table 3. Parameters of the model with a core, $\gamma = 0$, and an isotropic velocity field, $\beta = 0$, estimated with our MCMC analysis. The estimates are the medians of the posterior distributions. The uncertainties correspond to the 68% confidence intervals of the posterior distributions. N is the number of stars in the mock catalogue; σ_v is the uncertainty on the measure of each velocity component of the stars in the mock catalogues.

Parameter	Input value	σ_v (km/s)	$N = 100$	$N = 1000$	$N = 2000$	$N = 4000$	$N = 6000$
$\log_{10}\left(\frac{\rho_0}{10^7 M_\odot/\text{kpc}^3}\right)$	2.284	0.0	$0.66^{+1.07}_{-0.73}$	$1.22^{+0.60}_{-0.54}$	$2.17^{+0.29}_{-0.37}$	$1.97^{+0.29}_{-0.29}$	$2.15^{+0.21}_{-0.23}$
		1.0	$0.64^{+1.08}_{-0.74}$	$1.22^{+0.62}_{-0.60}$	$2.18^{+0.29}_{-0.38}$	$1.97^{+0.29}_{-0.30}$	$2.15^{+0.22}_{-0.23}$
		5.0	$0.99^{+1.20}_{-1.22}$	$1.49^{+0.78}_{-1.01}$	$2.25^{+0.29}_{-0.43}$	$2.10^{+0.34}_{-0.44}$	$2.17^{+0.29}_{-0.36}$
$\log_{10}\left(\frac{r_s}{\text{kpc}}\right)$	-0.824	0.0	$-0.21^{+0.31}_{-0.43}$	$-0.42^{+0.22}_{-0.24}$	$-0.79^{+0.14}_{-0.11}$	$-0.70^{+0.11}_{-0.11}$	$-0.78^{+0.09}_{-0.08}$
		1.0	$-0.20^{+0.31}_{-0.43}$	$-0.42^{+0.25}_{-0.24}$	$-0.80^{+0.14}_{-0.11}$	$-0.70^{+0.11}_{-0.11}$	$-0.78^{+0.09}_{-0.08}$
		5.0	$-0.55^{+0.49}_{-0.46}$	$-0.66^{+0.41}_{-0.30}$	$-0.94^{+0.16}_{-0.11}$	$-0.86^{+0.17}_{-0.12}$	$-0.90^{+0.13}_{-0.10}$
γ	0.0	0.0	$1.29^{+0.28}_{-0.65}$	$0.99^{+0.28}_{-0.46}$	$0.19^{+0.40}_{-0.40}$	$0.33^{+0.29}_{-0.36}$	$0.20^{+0.26}_{-0.28}$
		1.0	$1.30^{+0.28}_{-0.63}$	$0.99^{+0.30}_{-0.48}$	$0.19^{+0.41}_{-0.40}$	$0.33^{+0.29}_{-0.36}$	$0.20^{+0.26}_{-0.29}$
		5.0	$1.47^{+0.46}_{-0.79}$	$0.89^{+0.53}_{-0.77}$	$0.16^{+0.47}_{-0.43}$	$0.17^{+0.48}_{-0.48}$	$0.20^{+0.41}_{-0.40}$
β	0.0	0.0	$-0.37^{+0.22}_{-0.25}$	$-0.09^{+0.06}_{-0.06}$	$0.00^{+0.04}_{-0.04}$	$-0.01^{+0.03}_{-0.02}$	$0.00^{+0.02}_{-0.02}$
		1.0	$-0.38^{+0.22}_{-0.26}$	$-0.09^{+0.06}_{-0.06}$	$0.00^{+0.04}_{-0.04}$	$-0.01^{+0.03}_{-0.03}$	$0.00^{+0.02}_{-0.02}$
		5.0	$-0.88^{+0.51}_{-0.61}$	$-0.15^{+0.09}_{-0.10}$	$-0.02^{+0.06}_{-0.06}$	$-0.01^{+0.04}_{-0.04}$	$0.00^{+0.03}_{-0.03}$

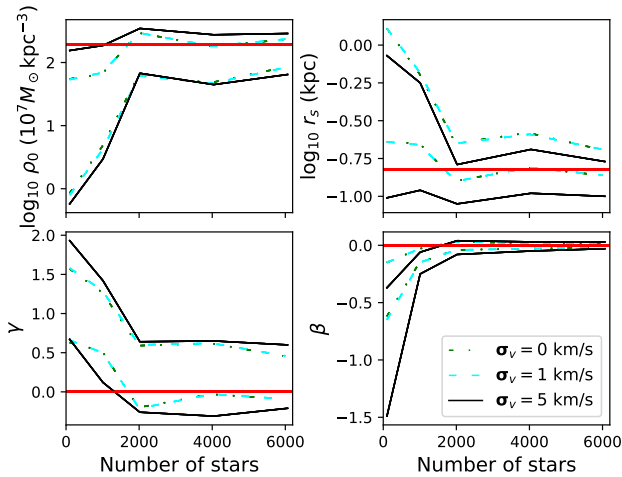


Figure 4. The 1σ confidence interval (upper and lower curves with the same style) of the parameter estimates as a function of the number of stars of the catalogue for a model with a core, $\gamma = 0$, and an isotropic velocity field, $\beta = 0$. Different line styles are for different velocity uncertainty σ_v , as listed in the inset. The red horizontal lines show the input parameters used to create the mock catalogues. The confidence intervals for $\sigma_v = 0 \text{ km s}^{-1}$ and $\sigma_v = 1 \text{ km s}^{-1}$ are indistinguishable.

core from a cusp. However, samples with smaller N return strongly biased values of the model parameters (see Sect. 4.1). Therefore, samples with $N < 2000$ stars are not recommended.

We conclude that our approach will be able to unambiguously distinguish between cusp and core models for a Draco-like galaxy if we measure the proper motions of at least 2000 stars, a sample size that is within the capability of future *Theia*-like astrometric missions (The *Theia* Collaboration et al. 2017; Malbet et al. 2021) or ground-based 30 meter class telescopes (Skidmore et al. 2015).

Our limit $N = 2000$ for the size of the star sample is larger than the limit derived by the analysis of Guerra et al. (2021) who find that $N = 1000$ is sufficient to distinguish between a core and a cusp at

Table 4. Same as Table 3 for models with either a core, $\gamma = 0$, or a cusp, $\gamma = 1$, and three different values of the velocity anisotropy parameter β . All the mock catalogues in this table contain $N = 2000$ stars and have velocity uncertainty $\sigma_v = 0 \text{ km s}^{-1}$. The input values of $\log_{10}(\rho_0/10^7 M_\odot/\text{kpc}^3)$ are [2.28, 0.73] for the models with a core and with a cusp, respectively. The input values of $\log_{10}(r_s/\text{kpc})$ are [-0.82, -0.10], respectively.

Parameters	Input β	Core ($\gamma = 0$)	Cusp ($\gamma = 1$)
$\log_{10}\left(\frac{\rho_0}{10^7 M_\odot/\text{kpc}^3}\right)$	-0.25	$2.04^{+0.30}_{-0.34}$	$0.71^{+0.21}_{-0.25}$
	0.0	$2.17^{+0.29}_{-0.37}$	$0.75^{+0.21}_{-0.24}$
	0.25	$2.51^{+0.18}_{-0.21}$	$0.43^{+0.27}_{-0.28}$
$\log_{10}\left(\frac{r_s}{\text{kpc}}\right)$	-0.25	$-0.76^{+0.13}_{-0.11}$	$-0.11^{+0.11}_{-0.09}$
	0.0	$-0.79^{+0.14}_{-0.11}$	$-0.10^{+0.11}_{-0.09}$
	0.25	$-0.90^{+0.08}_{-0.07}$	$0.03^{+0.13}_{-0.12}$
γ	-0.25	$0.40^{+0.32}_{-0.37}$	$1.08^{+0.10}_{-0.11}$
	0.0	0.19 ± 0.40	0.97 ± 0.12
	0.25	$-0.41^{+0.34}_{-0.32}$	$1.16^{+0.11}_{-0.12}$
β	-0.25	-0.35 ± 0.06	-0.32 ± 0.05
	0.0	0.0 ± 0.04	0.06 ± 0.04
	0.25	0.25 ± 0.03	0.21 ± 0.03

the 2σ confidence level. However, the result of Guerra et al. (2021) depends on the details of the density profile and such a distinction is thus not always guaranteed. Guerra et al. (2021) use a Fisher matrix formalism validated by the DYNESTY code (Speagle 2020), which is based on the dynamic nested sampling method of Higson et al. (2019). We use a traditional MCMC approach and we indeed confirm that a core and a cusp can in principle be separated with $N < 2000$ stars. However, as mentioned above, with these poorer samples the parameters of the density profile are strongly biased and we are unable to recover the correct mass density distribution and velocity anisotropy parameter.

The relevance of the measures of the proper motions is shown in Fig. 8. We show the results of the MCMC analysis of the mock catalogues with $N = 6000$ stars of the two models with a cusp or with a core where only the line-of-sight velocities of the stars

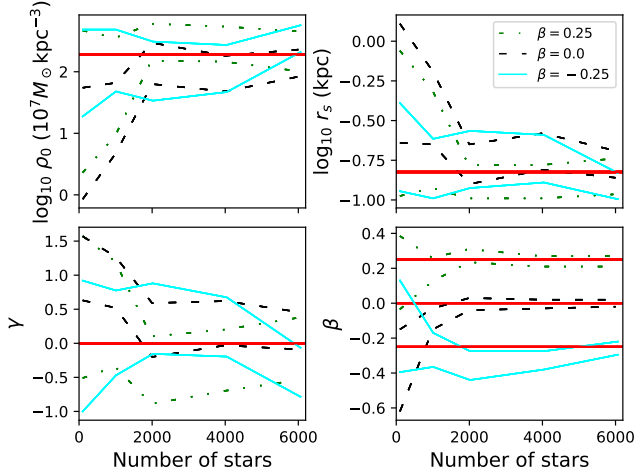


Figure 5. The 1σ confidence interval (upper and lower curves with the same style) of the parameter estimates as a function of the number of stars of the catalogue for models with a core, $\gamma = 0$, and three different values of the velocity anisotropy parameter β , as listed in the inset. The red horizontal lines show the input parameters used to create the mock catalogues. In these mock catalogues, the uncertainty on each velocity component of the individual stars is $\sigma_v = 0 \text{ km s}^{-1}$.

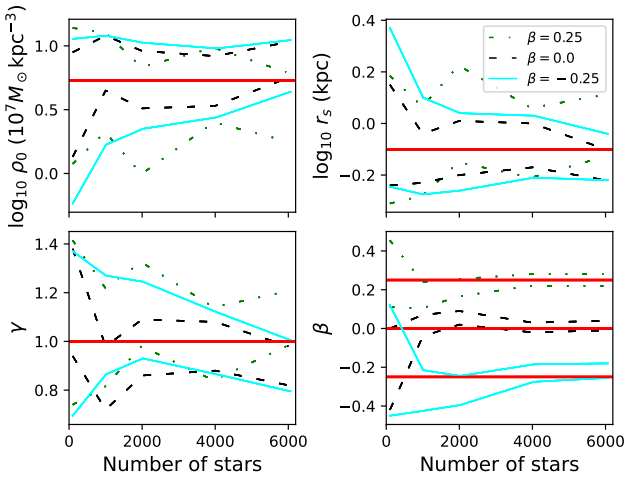


Figure 6. Same as Fig. 5 for models with a cusp, $\gamma = 1$.

are known. Compared to the case with $N = 6000$, where all the three velocity components are known (left panels of Fig. 7), the posterior distributions for the parameters γ and λ now degrade and become roughly comparable to the distributions for the catalogues with $N = 2000$ stars where all the three velocity components are known (right panels of Fig. 7). Nevertheless, the measure of λ can still distinguish the two models at more than 4σ . Samples with $N < 6000$ stars with unknown proper motions are thus unable to unambiguously distinguish between a core and a cusp.

We conclude that measuring the proper motions of the stars of a sample with $N \gtrsim 2000$ objects can efficiently assess whether the mass density profile has a central core or a cusp. In these analyses

Table 5. The estimated parameters of a model with a core, $\gamma = 0$, or a cusp, $\gamma = 1$, and an isotropic velocity field, $\beta = 0$. The input values of $\log_{10}(\rho_0/10^7 M_\odot \text{kpc}^{-3})$, $\log_{10}(r_s/\text{kpc})$, and of the log-slope estimated at the half-light radius $\lambda(a)$ are $[2.28; -0.82; 1.70]$ for the model with $\gamma = 0$ and $[0.73; -0.10; 1.40]$ for the model with $\gamma = 1$. In the models labeled “-3D”, all the three components of the velocity of each star are known. In the model labeled “-1D”, only the line-of-sight components of the velocities are known, whereas the proper motion components are missing.

Parameters	Input Model	Core ($\gamma = 0$)	Cusp ($\gamma = 1$)
$\log_{10}\left(\frac{\rho_0}{10^7 M_\odot/\text{kpc}^3}\right)$	2000-3D	$2.17^{+0.29}_{-0.37}$	$0.75^{+0.21}_{-0.24}$
	4000-3D	1.97 ± 0.29	$0.73^{+0.19}_{-0.20}$
	6000-3D	$2.15^{+0.21}_{-0.23}$	$0.90^{+0.13}_{-0.15}$
	6000-1D	$2.16^{+0.32}_{-0.41}$	$0.76^{+0.23}_{-0.29}$
$\log_{10}\left(\frac{r_s}{\text{kpc}}\right)$	2000-3D	$-0.79^{+0.14}_{-0.11}$	-0.11 ± 0.11
	4000-3D	-0.70 ± 0.11	-0.09 ± 0.09
	6000-3D	$-0.78^{+0.09}_{-0.08}$	-0.17 ± 0.06
	6000-1D	$-0.67^{+0.16}_{-0.12}$	0.0 ± 0.13
γ	2000-3D	0.19 ± 0.40	0.97 ± 0.11
	4000-3D	$0.33^{+0.29}_{-0.36}$	0.98 ± 0.10
	6000-3D	$0.20^{+0.26}_{-0.28}$	0.90 ± 0.08
	6000-1D	0.53 ± 0.36	1.14 ± 0.12
λ	2000-3D	1.73 ± 0.04	1.38 ± 0.04
	4000-3D	1.65 ± 0.03	1.37 ± 0.02
	6000-3D	1.71 ± 0.03	1.37 ± 0.02
	6000-1D	1.72 ± 0.07	1.45 ± 0.06

we adopted a null uncertainty σ_v on the measures of the velocity components: non-null uncertainties would leave the estimated values unbiased, but they would increase the uncertainties on the estimated γ and λ . The presence of a non-null uncertainty thus further increases the necessity of having a sufficiently large sample of stars with measured proper motions.

5 ESTIMATE OF THE MASS PROFILE OF THE DWARF

We now explore how the proper motions can improve the estimate of the mass profile of our synthetic dwarfs. We consider the model where the density profile has a core. The input parameters ρ_0 and r_s are listed in Table 1, in the column with $\gamma = 0$. The cumulative mass profile is provided by Eq. (3) and shown by the blue solid line in Fig. 9.

We now assume to observe this galaxy with the mock catalogue containing 6000 stars generated with the anisotropic velocity field $\beta = 0$ and null uncertainty $\sigma_v = 0 \text{ km s}^{-1}$ on the measures of the velocity components. The last column of Table 3 lists the four parameters estimated with our MCMC approach. The green open squares in Fig. 9 show the estimated mass profile. Increasing the uncertainty on the velocity components to $\sigma_v = 5 \text{ km s}^{-1}$ returns an estimated mass profile that is indistinguishable from the mass profile estimated when the uncertainties are null.

The velocity uncertainty propagates into the uncertainty on the mass profile. We estimate the 1σ confidence regions of the estimated mass profiles by carrying out 1,000 Monte Carlo simulations: we randomly select the parameters of the DM profile, (ρ_0, r_s, γ) , from the posterior distributions whose means and amplitudes are listed in Table 3. The result for $\sigma_v = 0 \text{ km s}^{-1}$ is shown in Fig. 9 as the area

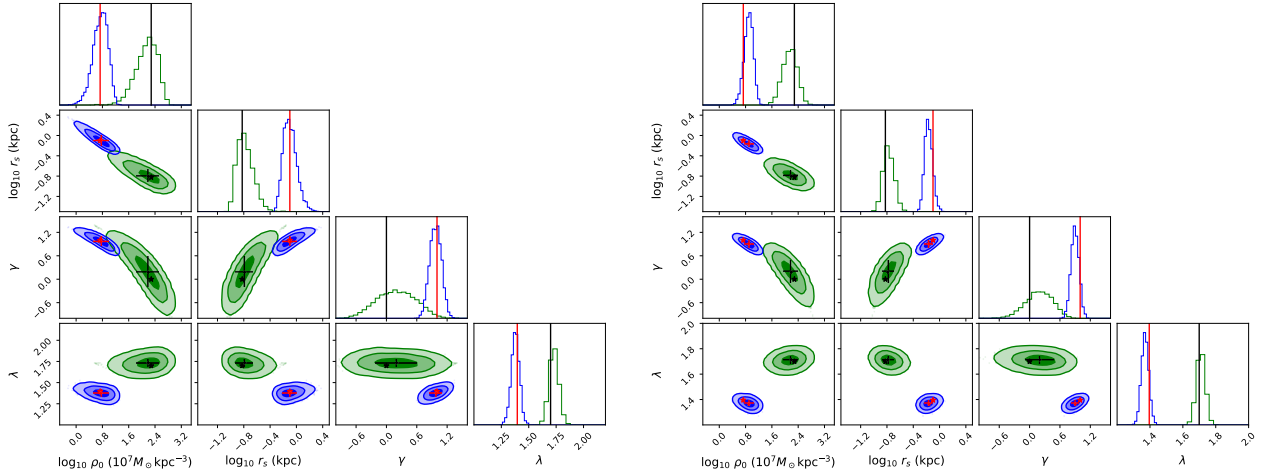


Figure 7. Posterior distributions of the estimated parameters of the DM density profiles of a dwarf model with a cusp (blue shaded areas) or a core (green shaded areas) and velocity anisotropy parameter $\beta = 0$. The left (right) panels show the posterior distributions derived from mock catalogues with $N = 6000$ ($N = 2000$) stars. We assume the uncertainty $\sigma_v = 0 \text{ km s}^{-1}$ on the stellar velocity components. The red and black solid stars and the red and black vertical lines indicate the input parameters of the models. The medians and the 68% confidence intervals of the posterior distributions are shown by the red and black dots with error bars and reported in Table 5. In this table, the MCMC analysis based on the mock catalogues with $N = 6000$ and $N = 2000$ stars are labeled 6000-3D and 2000-3D, respectively.

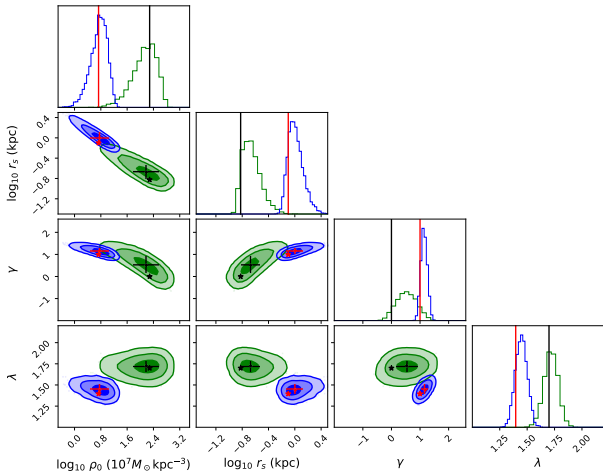


Figure 8. Same as Fig. 7 for a mock catalogue with $N = 6000$ stars where the proper motions of the stars are unavailable and only the line-of-sight components of the velocities are known. Input and estimated parameters for this model labeled 6000-1D are listed in Table 5.

bounded by the green solid lines. Adding the observational error on the velocities broadens the bounded area (green dotted lines).

The estimate of the mass profile substantially worsens when the proper motions are unavailable. The black crosses in Fig. 9 show the estimated mass profile when only the line-of-sight component of the velocities are known. For this estimated profile we use the parameters listed in Table 5 corresponding to the 6000-1D model. In this case, the mass profile is overestimated by a factor 2. In addition, when the proper motions are unavailable, we recover the model parameters within $\sim 2\sigma$, rather than $\sim 1\sigma$, and the uncertainties are a factor $\sim 1.5 - 2$ larger. This comparison quantifies the relevance of measuring the star proper motions to improve our knowledge of the DM distribution in dwarf galaxies.

This result is confirmed by the residuals between the true and

the estimated mass profiles shown in the bottom panel of Fig. 9. When the proper motions are available, the absolute values of the residuals range from a maximum of $\sim 9\%$ at $r \sim 0.05 \text{ kpc}$ to a minimum of $\sim 2.1\%$ at $r \sim 0.7 \text{ kpc}$, as shown by the green squares in the bottom panel of Fig. 9. When only the line-of-sight velocities are available, the absolute values of the residuals range from a maximum of $\sim 160\%$ at $r \sim 0.05 \text{ kpc}$ to a minimum of $\sim 97\%$ at $r \sim 0.45 \text{ kpc}$, as shown by the black crosses in the bottom panel of Fig. 9. We note that the residuals have a minimum close to the half-light radius of our model, in agreement with previous work (Strigari et al. 2007; Wolf et al. 2010; Walker et al. 2009; Guerra et al. 2021). The wide vertical scale of this panel inhibits the full appreciation of this minimum.

Finally, Fig. 10 shows the impact of the size of the star sample on the estimated mass profile. We show the cumulative mass profile estimated with a sample of 6000, 2000, and 100 stars with known proper motions and their corresponding 68% confidence regions: increasing the sample size narrows the 68% confidence region, whereas the residuals remain unaffected.

6 CONCLUSIONS

We determine the minimum number of stars and the minimum uncertainty on their measured proper motions that are necessary to distinguish between a cusp and a core in the dark matter density profile of a dwarf galaxy, based on kinematic information alone. We created a set of astrometric mock catalogues by adopting the dark matter parameters of an extended Navarro-Frenk-White model and the Plummer model of the stellar number density distribution of the Draco galaxy (Walker et al. 2009), which is a possible target of future space-borne astrometric missions (Malbet et al. 2016; Theia Collaboration et al. 2017; Malbet et al. 2019; Malbet et al. 2021).

The accuracy of the estimates of the parameters mostly depend on the size of the sample, whereas velocity uncertainties $\leq 5 \text{ km s}^{-1}$ only have a moderate impact on the parameter recovery. Our MCMC

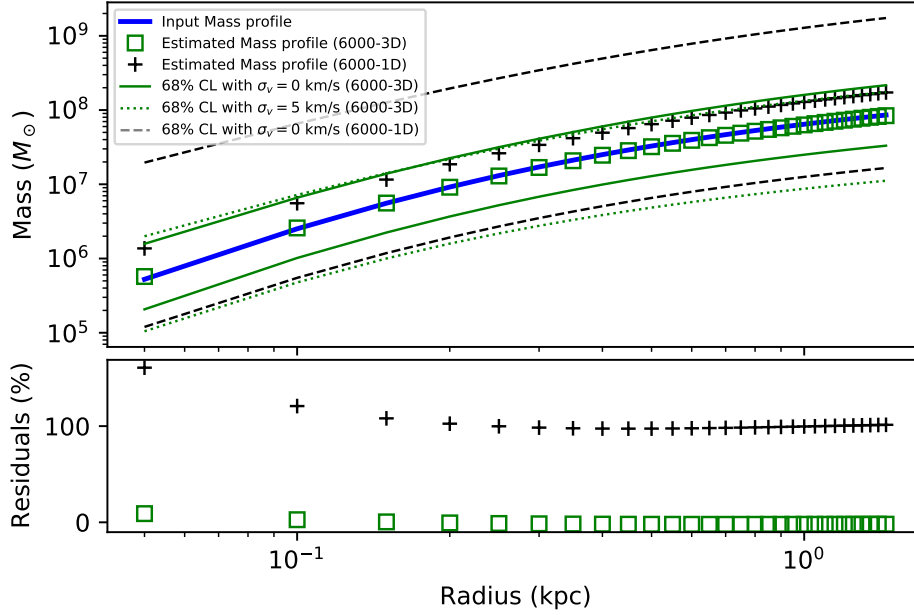


Figure 9. Effect of the knowledge of the proper motions on the mass estimate. *Upper panel:* Estimated cumulative mass profile of a dwarf model when the proper motions of 6000 stars are known (green open squares). The 68% confidence region is limited by the green solid (dotted) lines when the velocity uncertainties are $\sigma_v = 0$ (5) km s^{-1} . The solid blue line is the correct cumulative mass profile. The crosses show the estimated cumulative mass profile when only the line-of-sight component of the velocities are known. The black dashed lines limit the 68% confidence region in this case, when the velocity uncertainty is $\sigma_v = 0 \text{ km s}^{-1}$. *Lower panel:* Residuals between the true (blue solid line) and the estimated (green open squares or black crosses) cumulative mass profiles.

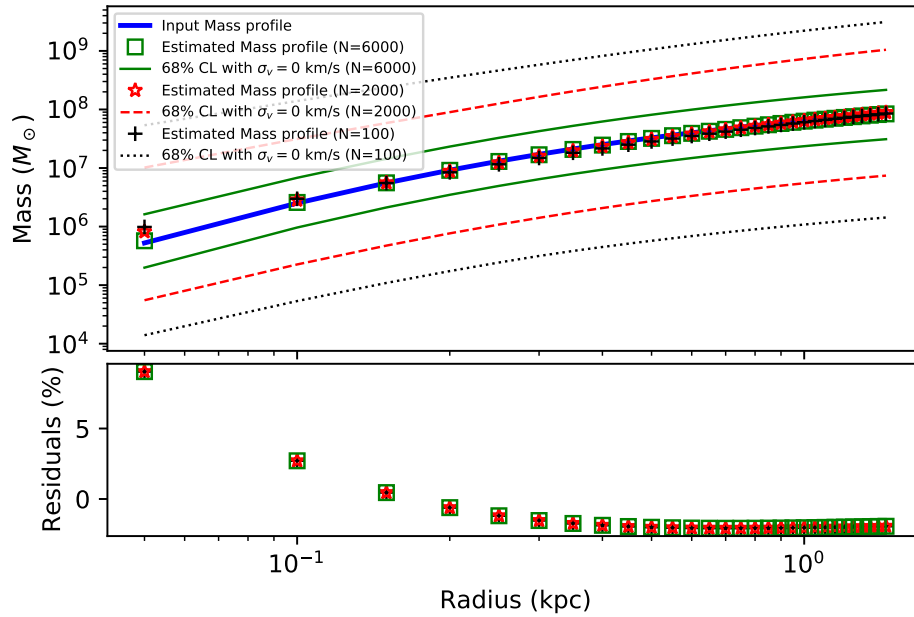


Figure 10. Effect of the size of the star sample on the mass estimate. *Upper panel:* Cumulative mass profile of a dwarf model estimated with a sample of 6000 (green open squares), 2000 (red stars), and 100 (black crosses) stars. The 68% confidence regions are limited by the green solid, red dashed, and black dotted lines, respectively. The uncertainty on the velocity components is $\sigma_v = 0 \text{ km s}^{-1}$. The blue solid line shows the true mass profile. *Lower panel:* Residuals between the true (blue solid line) and the estimated cumulative mass profiles. Symbols are as in the upper panel.

algorithm returns the dark matter parameters, including the velocity anisotropy parameter β , within $\sim 10\%$ of the true value and with a 1σ relative uncertainty $\lesssim 20\%$ for samples with $N \geq 2000$ stars.

With a sample of $N = 2000$ stars with measured proper motions, the measure of the log-slope $\lambda = -d \ln \rho / d \ln r$ of the density profile at the half-light radius distinguishes between a central core and a central cusp at more than 8σ in dwarfs described by our fiducial models (Strigari et al. 2007; Guerra et al. 2021). With the measure of the line-of-sight velocity components alone, the log-slope λ can still distinguish the two models at more than 4σ with a sample of at least $N = 6000$ stars. The validity of these results to dwarfs described by a more extended family of density profiles than we explored here remains to be investigated.

Proper motions enable the recovery of the cumulative mass profile of the dwarf with no bias with samples of stars as small as $N = 100$ stars. Increasing the sample size reduces the uncertainty on the mass: with $N = 6000$ stars the mass profile is on average 0.15 dex accurate.

In the future, we plan to investigate how the simplifying assumptions we adopted here can affect our results. Indeed, we assumed (1) a constant anisotropy parameter β rather than a radial dependent $\beta(r)$ (e.g., Okoli & Afshordi 2015), and (2) spherical symmetry for the synthetic dwarf, although real dwarfs appear elliptical on the sky (e.g., Irwin & Hatzidimitriou 1995; Salomon et al. 2015). Moreover, we assumed a simplified scheme for the uncertainty on the star velocities: we assumed the same error for the three components of the velocity, whereas, in reality, proper motions and line-of-sight velocities have substantially different uncertainties, as they depend on either astrometric or spectroscopic measurements. In addition, in our analysis we neglected the star brightness, which affects the uncertainties on the velocity components. Finally, we assumed null errors on the distance of the dwarf from the observer, and of the projected distance of the stars from the dwarf centre. More realistic mock catalogues will help to better quantify the constraints on the dynamical properties of dwarfs and on the nature of dark matter that can be obtained with 30 meter class telescopes (Skidmore et al. 2015), with future astrometric space missions aimed at measuring the positions of celestial objects with precision of the order of the micro-arcsecond (Malbet et al. 2016; The Theia Collaboration et al. 2017; Malbet et al. 2019; Malbet et al. 2021), or with a combination of the measures of these two classes of facilities (Evslin 2015).

ACKNOWLEDGEMENTS

We sincerely thank the active collaboration of Alistair Hodson during the initial development of this project. We are in debt with a referee whose insightful comments crucially improved our results. We acknowledge partial support from the INFN grant InDark and the Italian Ministry of Education, University and Research (MIUR) under the Departments of Excellence grant L.232/2016. IDM was supported by the grant “The Milky Way and Dwarf Weights with Space Scales” funded by University of Torino and Compagnia di S. Paolo (UniTO-CSP). IDM also acknowledges support from Ayuda IJCI2018-036198-I funded by MCIN/AEI/10.13039/501100011033 and FSE “El FSE invierte en tu futuro” o “Financiado por la Unión Europea “NextGenerationEU”/PRTR”. IDM is also supported by the project PGC2018-096038-B-I00 funded by the Spanish “Ministerio de Ciencia e Innovación” and FEDER “A way of making Europe”, and by the project SA096P20

Junta de Castilla y León. This research has made use of NASA’s Astrophysics Data System Bibliographic Services.

Data Availability Statement

No new data were generated or analysed in support of this research.

REFERENCES

- Akerib D. S., et al., 2017, *Phys. Rev. Lett.*, **118**, 021303
 Aprile E., et al., 2018, *Phys. Rev. Lett.*, **121**, 111302
 Bekenstein J., Milgrom M., 1984, *ApJ*, **286**, 7
 Benítez-Llambay A., Frenk C. S., Ludlow A. D., Navarro J. F., 2019, *MNRAS*, **488**, 2387
 Berezhiani L., Khoury J., 2015, *Phys. Rev. D*, **92**, 103510
 Bertone G., Hooper D., 2018, *Reviews of Modern Physics*, **90**, 045002
 Bertone G., Hooper D., Silk J., 2005, *Phys. Rep.*, **405**, 279
 Binney J., Tremaine S., 2008, *Galactic Dynamics: Second Edition*. Princeton University Press
 Bose S., et al., 2019, *MNRAS*, **486**, 4790
 Breddels M. A., Helmi A., 2013, *A&A*, **558**, A35
 Broadhurst T., de Martino I., Luu H. N., Smoot G. F., Tye S. H. H., 2020, *Phys. Rev. D*, **101**, 083012
 Bullock J. S., Boylan-Kolchin M., 2017, *ARA&A*, **55**, 343
 Caldwell N., et al., 2017, *ApJ*, **839**, 20
 Campbell D. J. R., et al., 2017, *MNRAS*, **469**, 2335–2360
 Carignan C., Beaulieu S., 1989, *ApJ*, **347**, 760
 Carignan C., Freeman K. C., 1988, *ApJ*, **332**, L33
 Chen S.-R., Schive H.-Y., Chiueh T., 2017, *MNRAS*, **468**, 1338
 De Blok W. J. G., McGaugh S. S., 1997, *MNRAS*, **290**, 533
 De Lorenzi F., et al., 2009, *MNRAS*, **395**, 76
 De Martino I., 2016, *Phys. Rev. D*, **93**, 124043
 De Martino I., 2020, *MNRAS*, **493**, 2373
 De Martino I., De Laurentis M., 2017, *Phys. Lett. B*, **770**, 440
 De Martino I., Chakrabarty S. S., Cesare V., Gallo A., Ostorero L., Diaferio A., 2020a, *Universe*, **6**, 107
 De Martino I., Broadhurst T., Henry Tye S. H., Chiueh T., Schive H.-Y., 2020b, *PDU*, **28**, 100503
 Del Popolo A., Le Delliou M., 2017, *Galaxies*, **5**, 17
 Di Cintio A., Brook C. B., Macciò A. V., Stinson G. S., Knebe A., Dutton A. A., Wadsley J., 2014, *MNRAS*, **437**, 415
 Di Valentino E., Melchiorri A., Silk J., 2020, *Nat. Astr.*, **4**, 196
 Ellis J., Hagelin J. S., Nanopoulos D. V., Olive K., Srednicki M., 1984, *Nuclear Physics B*, **238**, 453
 Evans A. J., Strigari L. E., Zivick P., 2022, *MNRAS*, **511**, 4251
 Evslin J., 2015, *MNRAS*, **452**, L41
 Famaey B., McGaugh S. S., 2012, *Living Reviews in Relativity*, **15**, 10
 Feng J. L., 2010, *ARA&A*, **48**, 495
 Foreman-Mackey D., Hogg D. W., Lang D., Goodman J., 2013, *PASP*, **125**, 306
 Freese K., 2017, *IJMPD*, **26**, 1730012
 Frenk C. S., White S. D. M., 2012, *Annalen der Physik*, **524**, 507
 Gaia Collaboration 2016, *VizieR Online Data Catalog*, p. I/337
 Gaia Collaboration et al., 2016a, *A&A*, **595**, A1
 Gaia Collaboration et al., 2016b, *A&A*, **595**, A2
 Gaia Collaboration et al., 2018a, *A&A*, **616**, A1
 Gaia Collaboration et al., 2018b, *A&A*, **616**, A12
 Gaia Collaboration et al., 2021, *A&A*, **649**, A1
 Gentile G., Salucci P., Klein U., Granato G. L., 2007, *MNRAS*, **375**, 199–212
 Governato F., et al., 2012, *MNRAS*, **422**, 1231
 Guerra J., Geha M., Strigari L. E., 2021, arXiv e-prints, p. arXiv:2112.05166
 Handley W., 2021, *Phys. Rev. D*, **103**, L041301
 Hernquist L., 1990, *ApJ*, **356**, 359

Higson E., Handley W., Hobson M., Lasenby A., 2019, *Statistics and Computing*, **29**, 891

Hu W., Barkana R., Gruzinov A., 2000, *Phys. Rev. Lett.*, **85**, 1158

Irwin M., Hatzidimitriou D., 1995, *MNRAS*, **277**, 1354

Lokas E. L., 2002, *MNRAS*, **333**, 697

Lokas E. L., Mamon G., 2003, *MNRAS*, **343**, 401

Luongo O., Muccino M., Colgáin E. Ó., Sheikh-Jabbari M. M., Yin L., 2021, arXiv e-prints, p. arXiv:2108.13228

Malbet F., et al., 2016, in MacEwen H. A., Fazio G. G., Lystrup M., Batalha N., Siegler N., Tong E. C., eds, Society of Photo-Optical Instrumentation Engineers (SPIE) Conference Series Vol. 9904, Space Telescopes and Instrumentation 2016: Optical, Infrared, and Millimeter Wave. p. 99042F, doi:10.1117/12.2234425

Malbet F., et al., 2019, arXiv e-prints, p. arXiv:1910.08028

Malbet F., et al., 2021, *Experimental Astronomy*, **51**, 845

Marsh D. J. E., Pop A.-R., 2015, *MNRAS*, **451**, 2479

Mashchenko S., Wadsley J., Couchman H. M. P., 2008, *Science*, **319**, 174

Massari D., Breddels M. A., Helmi A., Posti L., Brown A. G. A., Tolstoy E., 2018, *Nat. Astr.*, **2**, 156

Massari D., Helmi A., Mucciarelli A., Sales L. V., Spina L., Tolstoy E., 2020, *A&A*, **633**, A36

Mateo M. L., 1998, *ARA&A*, **36**, 435

Mathews G. J., et al., 2020, Cosmological Solutions to the Lithium Problem. (<https://journals.jps.jp/doi/pdf/10.7566/JPSCP.31.011033>), doi:10.7566/JPSCP.31.011033, <https://journals.jps.jp/doi/abs/10.7566/JPSCP.31.011033>

McConnachie A. W., 2012, *AJ*, **144**, 4

McGaugh S., 2020, *Galaxies*, **8**, 35

Milgrom M., 1983, *ApJ*, **270**, 365

Napolitano N. R., Pota V., Romanowsky A. J., Forbes D. A., Brodie J. P., Foster C., 2014, *MNRAS*, **439**, 659

Navarro J. F., Frenk C. S., White S. D. M., 1997, *ApJ*, **490**, 493

Oñorbe J., Boylan-Kolchin M., Bullock J. S., Hopkins P. F., Kereš D., Faucher-Giguère C.-A., Quataert E., Murray N., 2015, *MNRAS*, **454**, 2092

Oh S.-H., et al., 2015, *The Astronomical Journal*, **149**, 180

Okoli C., Afshordi N., 2015, *MNRAS*, **456**, 3068–3078

Planck Collaboration et al., 2016, *A&A*, **594**, A16

Planck Collaboration et al., 2020, *A&A*, **641**, A1

Plummer H. C., 1911, *MNRAS*, **71**, 460

Pontzen A., Governato F., 2012, *MNRAS*, **421**, 3464

Pozo A., Broadhurst T., de Martino I., Luu H. N., Smoot G. F., Lim J., Neyrinck M., 2021, *MNRAS*, **504**, 2868

Primack J. R., 2012, *Annalen der Physik*, **524**, 535

Read J. I., Steger P., 2017, *MNRAS*, **471**, 4541

Read J. I., Agertz O., Collins M. L. M., 2016, *MNRAS*, **459**, 2573

Read J. I., Walker M. G., Steger P., 2018, *MNRAS*, **481**, 860

Richardson T., Fairbairn M., 2013, arXiv e-prints, p. arXiv:1305.0670

Richardson T. D., Spolyar D., Lehnert M. D., 2014, *MNRAS*, **440**, 1680

Riess A. G., et al., 2016, *ApJ*, **826**, 56

Riess A. G., Casertano S., Yuan W., Macri L. M., Scolnic D., 2019, *ApJ*, **876**, 85

Rocha M., Peter A. H. G., Bullock J. S., Kaplinghat M., Garrison-Kimmel S., Oñorbe J., Moustakas L. A., 2013, *MNRAS*, **430**, 81

Salomon J.-B., Ibata R. A., Martin N. F., Famaey B., 2015, *MNRAS*, **450**, 1409

Salucci P., 2018, *Foundations of Physics*, **48**, 1517–1537

Schoeck M., Do T., Ellerbroek B., Herriot G., Meyer L., Suzuki R., Wang L., Yelda S., 2013, in Esposito S., Fini L., eds, Proceedings of the Third AO4ELT Conference. p. 77, doi:10.12839/AO4ELT3.13356

Schwarz D. J., Copi C. J., Huterer D., Starkman G. D., 2016, *Classical and Quantum Gravity*, **33**, 184001

Skidmore W., TMT International Science Development Teams Science Advisory Committee T., 2015, *Research in Astronomy and Astrophysics*, **15**, 1945

Speagle J. S., 2020, *MNRAS*, **493**, 3132

Spekkens K., Giovanelli R., Haynes M. P., 2005, *The Astronomical Journal*, **129**, 2119

Spergel D. N., Steinhardt P. J., 2000, *Phys. Rev. Lett.*, **84**, 3760

Strigari L. E., Bullock J. S., Kaplinghat M., 2007, *ApJ*, **657**, L1

Tanabashi M., et al., 2018, *Phys. Rev. D*, **98**, 030001

The Theia Collaboration et al., 2017, arXiv e-prints, p. arXiv:1707.01348

Torrealba G., Koposov S. E., Belokurov V., Irwin M., 2016, *MNRAS*, **459**, 2370

Torrealba G., et al., 2019, *MNRAS*, **488**, 2743

Van den Bosch F. C., Swaters R. A., 2001, *MNRAS*, **325**, 1017–1038

Walker M. G., Peñarrubia J., 2011, *ApJ*, **742**, 20

Walker M. G., Mateo M., Olszewski E. W., Peñarrubia J., Evans N. W., Gilmore G., 2009, *ApJ*, **704**, 1274

Watkins L. L., van de Ven G., den Brok M., van den Bosch R. C. E., 2013, *MNRAS*, **436**, 2598

Webb J. J., Vesperini E., 2018, *MNRAS*, **479**, 3708

Weinberg D. H., Bullock J. S., Governato F., Kuzio de Naray R., Peter A. H. G., 2015, *Proceedings of the National Academy of Science*, **112**, 12249

Wolf J., Martinez G. D., Bullock J. S., Kaplinghat M., Geha M., Muñoz R. R., Simon J. D., Avedo F. F., 2010, *MNRAS*, **406**, 1220

Zhao H., 1996, *MNRAS*, **278**, 488

Zhu L., et al., 2016a, *MNRAS*, **462**, 4001

Zhu L., van de Ven G., Watkins L. L., Posti L., 2016b, *MNRAS*, **463**, 1117

APPENDIX A: RELATIONS BETWEEN SPHERICAL AND CARTESIAN COORDINATE SYSTEMS

For completeness, we remind the formulae used to transform, in the reference frame centered on the centre of mass of the dwarf galaxy, the mean velocity μ , the covariance matrix C , and the likelihood function in Eq. (19), presented in Sect. 2.3, from the system of spherical coordinates (r, θ, ϕ) to the system of Cartesian coordinates (x, y, z) . The transformation equation is

$$\begin{pmatrix} v_x \\ v_y \\ v_z \end{pmatrix} = \hat{R} \begin{pmatrix} v_r \\ v_\theta \\ v_\phi \end{pmatrix}, \quad (\text{A1})$$

where the rotation matrix \hat{R} is

$$\hat{R} = \begin{pmatrix} \cos \phi \sin \theta & \cos \theta \cos \phi & -\sin \phi \\ \sin \theta \sin \phi & \cos \theta \sin \phi & \cos \phi \\ \cos \theta & -\sin \theta & 0 \end{pmatrix}. \quad (\text{A2})$$

In the spherical coordinate system, for non-rotating spherically symmetric systems, the first moments of the distributions of the three velocity components v_r , v_ϕ , and v_θ are null. Similarly, all the mixed terms of the form $\overline{v_r v_\phi}$ are null. In the Cartesian coordinates, we thus have

$$\overline{v_x} = 0 \quad (\text{A3})$$

$$\overline{v_y} = 0 \quad (\text{A4})$$

$$\overline{v_z} = 0, \quad (\text{A5})$$

and

$$\overline{v_x^2} = \cos^2 \phi \left(\overline{v_r^2} \sin^2 \theta + \overline{v_\phi^2} \cos^2 \theta \right) + \overline{v_\theta^2} \sin^2 \phi \quad (\text{A6})$$

$$\overline{v_y^2} = \sin^2 \phi \left(\overline{v_r^2} \sin^2 \theta + \overline{v_\phi^2} \cos^2 \theta \right) + \overline{v_\theta^2} \cos^2 \phi \quad (\text{A7})$$

$$\overline{v_z^2} = \overline{v_r^2} \cos^2 \theta + \overline{v_\phi^2} \sin^2 \theta \quad (\text{A8})$$

$$\overline{v_x v_y} = (\overline{v_r^2} - \overline{v_\phi^2}) \cos \phi \cos \theta \sin \theta \quad (\text{A9})$$

$$\overline{v_x v_z} = \sin^2 \phi \left(\overline{v_r^2} \sin^2 \theta + \overline{v_\phi^2} \cos^2 \theta \right) + \overline{v_\phi^2} \cos^2 \phi \quad (\text{A10})$$

$$\overline{v_y v_z} = -\frac{1}{2} \left(\overline{v_r^2} - \overline{v_\phi^2} \right) \sin(2\theta) \sin \phi. \quad (\text{A11})$$

This paper has been typeset from a \TeX/L\AA\TeX file prepared by the author.